



A new magnetic nano zero-valent iron encapsulated in carbon spheres for oxidative degradation of phenol

Yuxian Wang, Hongqi Sun*, Xiaoguang Duan, Ha Ming Ang, Moses O. Tadé,
Shaobin Wang*

Department of Chemical Engineering and CRC for Contamination Assessment and Remediation of the Environment (CRC CARE), Curtin University,
GPO Box U1987, WA 6845, Australia



ARTICLE INFO

Article history:

Received 5 November 2014
Received in revised form 23 January 2015
Accepted 14 February 2015
Available online 17 February 2015

Keywords:

Carbon nanosphere
Zero-valent iron
Magnetic nanoparticle
Catalytic oxidation
Phenol

ABSTRACT

In this study, magnetic carbon encapsulated nano iron hybrids (nano $\text{Fe}^0/\text{Fe}_3\text{C}@\text{CS}$) were synthesized via a novel one-pot hydrothermal method followed by self-reduction in N_2 atmosphere. The structural, morphological, and physicochemical properties of the samples were thoroughly investigated by X-ray diffraction (XRD), field emission scanning electron microscopy (FE-SEM), N_2 sorption isotherms and thermogravimetric analysis–differential scanning calorimetry (TGA–DSC). Catalytic performance of the as-synthesized nanoparticles was tested in activation of oxone® for phenol degradation in aqueous solutions. Superior catalytic performance was observed by complete removal of 20 ppm phenol within 10 min. The formation of Fe_3C was found to contribute to a better stability and magnetic separation of $\text{Fe}^0/\text{Fe}_3\text{C}@\text{CS}$ in its repeated uses. Both electron paramagnetic resonance (EPR) and classic quenching tests were carried out to investigate the mechanism of radical generation and evolution in phenol oxidation. Different from Co- and Mn-based catalysts in generation of sulfate radicals, $\text{Fe}^0/\text{Fe}_3\text{C}@\text{CS}$ selectively induced hydroxyl radicals for phenol degradation.

© 2015 Elsevier B.V. All rights reserved.

1. Introduction

Rapid developments in industrialization, population expansion and urbanization have resulted in vast pollutants to be discharged to water body, which has attracted great public concerns in recent years. Among the wide variety of aqueous pollutants, organic compounds are a major contribution to wastewater. Most of organic compounds in wastewater impose detrimental effects to human health and the eco-environment, and are resistant to natural degradation, so intensive scientific research interests have been focused on complete decomposition of the organic pollutants. In the past few years, advanced oxidation processes (AOPs) utilizing very reactive species such as hydroxyl radicals ($\cdot\text{OH}$), have been developed as an effective approach for organic abatement [1–3]. As one of the most prevalent AOPs, Fenton or Fenton-like reactions using Fe (II or III) to produce hydroxyl radicals have been proven as a cost-effective technology [3]. However, metal leaching, large quantity of sludge and low pH (2–4) limit their further application [4]. Recently,

sulfate radicals have been proposed as an alternative to hydroxyl radicals for organic oxidation. Generation of sulfate radicals can be achieved by heat, light radiation, and metal activation of sulfate oxidants, such as peroxyomonosulfate (PMS) [5–10].

Due to low cost and strong redox potential, zero-valent iron (ZVI) has been widely applied for removal of a variety of pollutants such as chlorinated hydrocarbons, nitrobenzenes, chlorinated phenols, polychlorinated biphenyls (PCBs), heavy metals, and various anions [11,12]. Compared with bulk ZVI, nanoscaled ZVI (nano- Fe^0) shows a higher activity in reduction reactions due to its high specific surface area and surface reactivity [13]. However, nano- Fe^0 suffers from poor air stability due to its high surface energy [14,15]. To improve the stability, it was suggested that nano- Fe^0 can be encapsulated into porous carbon spheres for enhancement of transportation and suspension, without significantly sacrificing activity [16]. Another concern to nano- Fe^0 particles is that they favor strong aggregation due to their strong inter-particle dipole–dipole attraction and the high surface area to volume ratio [17]. Therefore, for a better distribution, various types of support materials have been employed, such as bentonite [18], activated carbon [19], alumina [20] and polystyrene resin [21], etc. In general, borohydride salt was used in liquid-phase reduction methods for preparation of most of the supported nano- Fe^0 composites [18–20]. Nevertheless,

* Corresponding authors. Tel.: +61 892663776; fax: +61 892662681.

E-mail addresses: h.sun@curtin.edu.au (H. Sun), [\(S. Wang\).](mailto:shaobin.wang@curtin.edu.au)

vacuum operation, N_2 atmosphere, massive production of hydrogen and high cost of borohydride in the synthesis make such processes complex and cost-intensive.

Recently, we discovered that nano- Fe^0 encapsulated in microscaled carbon spheres ($Fe^0@CS$) can activate PMS to produce sulfate radicals for phenol degradation [22]. However, catalytic stability of the nanocomposites was below anticipation due to the rapid consumption of nano- Fe^0 in acid condition. In this study, a novel magnetic carbon encapsulated nano Fe^0/Fe_3C was fabricated by an *in situ* hydrothermal carbonization of glucose with addition of melamine, followed by a self-reduction in N_2 atmosphere. Owing to the emerging phase of Fe_3C , the as-synthesized $Fe^0/Fe_3C@CS$ catalyst showed a much higher stability than reported $Fe^0@CS$ [22]. Electron paramagnetic resonance (EPR) spectra suggested that hydroxyl radicals were selectively produced during the heterogeneous PMS activation, indicating an alternative to homogeneous Fenton reaction. Moreover, the prepared catalysts showed both high activity and magnetic separation efficiency in catalytic oxidation of phenol solutions.

2. Experimental

2.1. Chemicals and materials

Iron (II) chloride tetrahydrate (99.9%), iron(III) hexahydrate (99.9%) and melamine (99.8%) were purchased from Sigma–Aldrich. D-Glucose (99.9%) was obtained from Fluka. Ammonia solution (28%) was obtained from Ajax Finechem. High purity nitrogen gas (99.999%) was received from BOC. All chemicals were used as received without further purification.

2.2. Synthesis of magnetic carbon encapsulated Fe^0

Magnetic $Fe^0/Fe_3C@CS$ was synthesized via a modified hydrothermal method. In a typical synthesis, 2.52 g (0.02 mol) melamine and 7.24 g (0.02 mol) D-glucose were dissolved in 50 mL of ultrapure water. Then 5.41 g (0.02 mol) of $FeCl_3 \cdot 6H_2O$ and 2.01 g (0.01 mol) of $FeCl_2 \cdot 4H_2O$ were dissolved in the D-glucose/melamine solution, followed by 1 h stirring. Under vigorous stirring, 28% ammonia solution was added dropwisely at a rate of 0.5 mL/min under nitrogen flow (40 mL/min) to make solution pH reach 10. The mixed solution was then transferred into a Teflon-lined autoclave (120 mL) and treated in an oven at 180 °C for 18 h. After naturally cooling to room temperature, the obtained black suspension was filtered and washed by ethanol/water for three cycles. The precipitate was dried in an oven at 80 °C and labelled as $Fe^x@CS$. The dried samples were further annealed in N_2 atmosphere in a tubular furnace at 350, 550 and 750 °C for 4 h and then were accordingly denoted as $Fe^x@CS$ -350, $Fe^0/Fe_3C@CS$, and $Fe^x@CS$ -750, respectively. Nano- $Fe^0@CS$ was prepared as a reference material according to our previous study [22].

2.3. Characterization of materials

The morphology and composition of the catalysts were analyzed on a ZEISS NEON 40EsB scanning electron microscope (SEM) equipped with an energy dispersive spectrometer (EDS). XRD patterns were obtained on a Bruker D8 (Bruker-AXS, Karlsruhe, Germany) diffractometer using filtered $Cu K\alpha$ radiation ($=1.5418 \text{ \AA}$) with an accelerating voltage of 40 kV and current of 30 mA. N_2 adsorption/desorption was measured using a micromeritics tristar 3000 to evaluate porous structure and Brunauer–Emmett–Teller (BET) specific surface area. Prior to measurement the samples were degassed at 120 °C for 5 h in vacuum condition. The iron content and thermal stability of $Fe^x@CS$ were investigated using thermogravimetric analysis-differential scanning calorimetry (TGA-DSC)

in argon or air on a Mettler-Toledo stare system. The argon/air flow rate was set to be 100 mL/min and the heating rate was 10 °C/min. X-ray photoelectron spectroscopy (XPS) was conducted on a thermo escalab 250 with $Al K\alpha$ X-ray to investigate the chemical states of elements. A Shirley background was first subtracted followed by component fitting using Voigt functions with a 30% Lorentzian component.

2.4. Catalytic activity tests

The catalytic oxidation of phenol was carried out in a 500 mL reactor containing 20 ppm of phenol solution with a constant stirring at 400 rpm. The reactor was attached to a stand and dipped in a water bath with a temperature controller. Unless specifically stated, the reaction temperature was 25 °C. In a typical test, firstly, 0.1 g catalyst was added into the phenol solution for 30 min to achieve adsorption–desorption equilibrium, then Oxone® (2KHSO₅·KHSO₄·K₂SO₄, PMS, obtained from Aldrich) was added into the solution at 2.0 g/L. At a certain time interval, 1 mL sample was withdrawn by a syringe and filtered into a vial, which was pre-filled with 0.5 mL of methanol to quench the reaction. The concentration of phenol was analyzed using a Varian high performance liquid-chromatography (HPLC) with a UV detector set at 270 nm. A C-18 column was used to separate the organics while the mobile phase made of 30% CH_3CN and 70% water was at a flow rate of 1 mL/min. For catalytic phenol degradation, each experiment was repeated in order to obtain error bars on the plots.

3. Results and discussion

3.1. Physicochemical properties of the materials

Fig. 1 illustrates XRD patterns of the as-prepared nanocomposites. For $Fe^x@CS$, cubic structured γ - Fe_2O_3 (JCPDS no. 39-1346) with lattice constant of 8.3248 Å was discerned by the observation of diffraction peaks at 31.1, 35.6, 43.1, 57.9 and 62.5° [23]. These peaks are corresponding to the crystal planes of (2 2 0), (3 1 1), (4 0 0), (4 2 2) and (4 4 0), respectively. Besides, the diffraction peak located at 27.3° indicated the formation of $g-C_3N_4$ [24]. Since no obvious peak from graphite (ca. $2\theta = 26^\circ$) was present, the produced carbon was suggested to be amorphous. For $Fe^0/Fe_3C@CS$, after thermal treatments under nitrogen, the diffraction peaks of γ - Fe_2O_3 became very weak, and the peak of $g-C_3N_4$ disappeared. Diffraction peaks formed at around 45.1° confirmed the formation of zero-valent iron and Fe_3C [25]. According to the Scherrer's formula, the average grain size of the zero-valent iron particles was calculated to be 26 nm. The changes observed in XRD patterns before and after

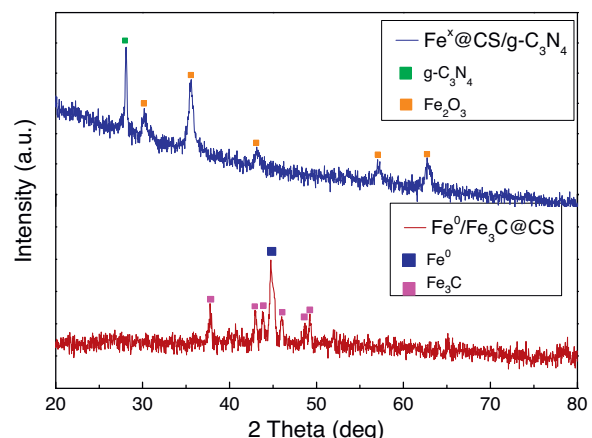


Fig. 1. XRD patterns of $Fe^x@CS$ and $Fe^0/Fe_3C@CS$ composites.

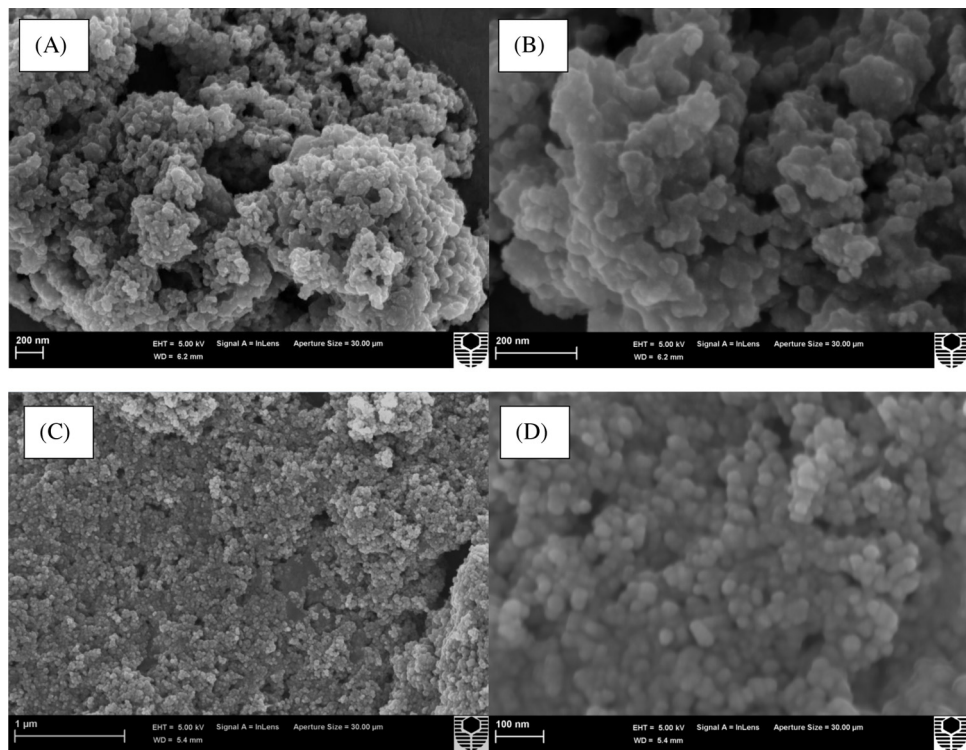


Fig. 2. SEM images of $\text{Fe}^x@\text{CS}$ (A) and (B), and $\text{Fe}^0/\text{Fe}_3\text{C}@\text{CS}$ (C) and (D).

calcination indicated that a solid-state pyrolysis process occurred and Fe_2O_3 , carbon and $\text{g-C}_3\text{N}_4$ reacted with each other to form zero-valent iron and Fe_3C compound [25].

Structure and morphology of the as-prepared samples were investigated by SEM images, as shown in Fig. 2. Before calcination (Fig. 2(A)), these nanoparticles were highly agglomerated due to the magnetic dipole interaction of $\gamma\text{-Fe}_2\text{O}_3$ nanoparticles and the high surface energy caused by the nano-scaled size [26]. From the magnification image (Fig. 2(B)), plate-like morphology with the average size of 50–100 nm was observed, which could be assigned to the 2D structure of the graphitic carbon nitride ($\text{g-C}_3\text{N}_4$) [24]. While the irregular protrudes attached on the 2D plates could be ascribed to the carbonized glucose and the $\gamma\text{-Fe}_2\text{O}_3$ nanoparticles. After calcination in nitrogen atmosphere (Fig. 2(C) and (D)), the 2D plate-like morphology disappeared and regular nanospheres were formed with a diameter around 20–30 nm, which was in agreement with the result obtained from XRD pattern using the Scherrer's formula. The transformation of the morphology suggested that most of the carbonized glucose and $\text{g-C}_3\text{N}_4$ had been reacted with Fe_2O_3 to form zero-valent iron, showing good accordance with the changes discovered in XRD patterns.

N_2 sorption isotherms and pore size distributions of the samples were evaluated through N_2 adsorption/desorption (Fig. 3). Both samples presented a type IV isotherm with a type H3 hysteresis loop, suggesting a typical mesoporous structure in accordance with the classification of IUPAC [27]. As seen in Fig. 3(A), $\text{Fe}^x@\text{CS}$ displayed a narrow hysteresis loop at a relative pressure P/P_0 range of 0.85–0.99. However, the hysteresis loop on $\text{Fe}^0/\text{Fe}_3\text{C}@\text{CS}$ was much broader, ranging from 0.45 to 0.99, as shown in Fig. 3(B), indicating a more porous structure and thus a larger surface area and pore volume. The BET surface area of $\text{Fe}^0/\text{Fe}_3\text{C}@\text{CS}$ was twice greater than that of $\text{Fe}^x@\text{CS}$ ($42.3 \text{ m}^2/\text{g}$ vs. $18.0 \text{ m}^2/\text{g}$) and the pore volumes of the sample with/without calcination were 0.19 and $0.043 \text{ cm}^3/\text{g}$, respectively. The vast difference in surface area or pore volume between the two samples might be owed to the calcination process which could produce porous structures. In terms of

pore size distributions, $\text{Fe}^x@\text{CS}$ (Fig. 3(A)) displayed a bimodal pore size distribution, centered at 0.5 and 26 nm, respectively. While $\text{Fe}^0/\text{Fe}_3\text{C}@\text{CS}$ showed a single modal pore size distribution concentrated at around 2.5 nm.

Fig. 4 displays TG-DSC profiles of $\text{Fe}^x@\text{CS}$ in argon and air. Fig. 4(A) shows the phase transformation of iron species under an argon atmosphere. As seen, three endothermic peaks were observed at 387, 514 and 573 °C, respectively. The first endothermic peak at 387 °C was attributed to the transformation of $\gamma\text{-Fe}_2\text{O}_3$ to Fe_3O_4 , while the peak at 514 °C could be assigned to the reduction of Fe_3O_4 to Fe^0 [28]. The third endothermic peak centering at 573 °C could be ascribed to the formation of Fe_3C , which was also shown in the XRD result. Fig. 4(B) shows the combustion performance of $\text{Fe}^x@\text{CS}$ under air. Two exothermic peaks were found at 200–380 °C, which could be attributed to the decomposition and combustion of organic and amorphous carbons, respectively [29]. When temperature was elevated above 450 °C, weight loss was stabilized and was determined to be 43.0%, suggesting the complete combustion of amorphous carbon and oxidation of iron.

3.2. Catalytic oxidation of phenol

To investigate the catalytic activities of the samples, control experiments were firstly carried out in terms of catalyst adsorption and PMS self-oxidation. Fig. 5 displays the adsorption and phenol degradation profiles on various samples. When PMS alone was added to the phenol solution, less than 10% phenol was degraded, revealing that PMS could not be effectively activated by ambient temperature. For adsorption tests, when the $\text{Fe}^x@\text{CS}$ and $\text{Fe}^0/\text{Fe}_3\text{C}@\text{CS}$ samples were added to the phenol without the presence of PMS, insignificant phenol removal was observed on both samples, indicating that phenol removal by adsorption was negligible. For catalytic reactions, $\text{Fe}^x@\text{CS}$ was tested first for activation of PMS to produce reactive species to degrade phenol. As seen, around 20% phenol was degraded within 180 min. Our previous studies have showed that neither Fe_3O_4 nor Fe_2O_3 has notable catalytic

activity in PMS activation [22]. While $\text{Fe}^0/\text{Fe}_3\text{C}@\text{CS}$ provided a much fast catalytic activity, and 100% removal of phenol was achieved within 10 min. In the meantime, nano- $\text{Fe}^0@\text{CS}$ prepared according to a previous study [22] was also tested in activation of PMS for phenol degradation. It was found that, under the same conditions, complete phenol removal was only achieved within 30 min, revealing an inferior catalytic activity than $\text{Fe}^0/\text{Fe}_3\text{C}@\text{CS}$ synthesized in this study. These results strongly suggested that the nanoscaled ZVI had a superior catalytic activity and could activate PMS efficiently to produce reactive species for phenol degradation.

Fig. S2 displays the phenol removal induced by the prepared $\text{Fe}^0/\text{Fe}_3\text{C}$ catalysts. As shown, these catalysts presented insignificant adsorption at less than 5% removal within 60 min. For catalytic oxidation, $\text{Fe}^x@\text{CS}-350$ was able to degrade around 30% phenol in 60 min. However, for both $\text{Fe}^0/\text{Fe}_3\text{C}@\text{CS}$ and $\text{Fe}^x@\text{CS}-750$, complete phenol degradation was achieved within 10 min. XPS Fe 2p spectra of the three catalysts were shown in Fig. S3. For $\text{Fe}^x@\text{CS}-350$ (Fig. S3(A)), besides the characteristic peaks of oxidized Fe(III) (711 eV and 724 eV) [30,31], a weak peak (707 eV) from elemental Fe was observed with the composition of 0.9 at.% [32,33]. No Fe_3C characteristic peak (720 eV) was observed [33]. Annealing at 350 °C might converted Fe(III) to FeOOH or Fe_2O_3 with trace Fe^0 , phenol degradation might arise from the low catalytic activity of Fe_2O_3 [22]. TG-DSC analysis suggested that when calcination temperature was above 514 °C, iron oxides would be transformed to Fe^0 by the reduction of carbon. Moreover, Fe_3C would gradually form. Fig. S3(B) shows the Fe 2p spectrum of $\text{Fe}^0/\text{Fe}_3\text{C}@\text{CS}$. As seen, notable peaks at 707 eV and 720 eV for Fe^0 and Fe_3C , respectively, were appearing, consistent with TG-DSC analysis. Fe^0 and Fe_3C contents were determined to be 20.4 at.% and 14.7 at.%, respectively.

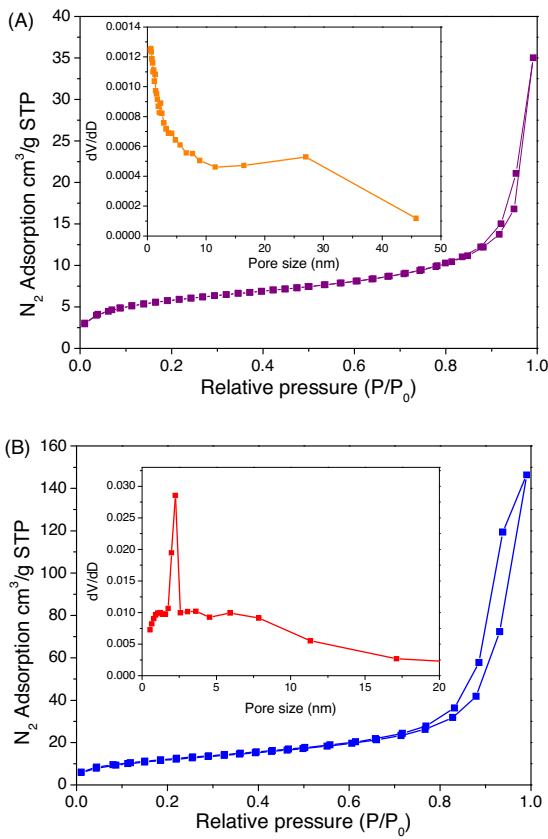


Fig. 3. Nitrogen sorption isotherms and pore size distributions of the samples. (A) $\text{Fe}^x@\text{CS}$ and (B) $\text{Fe}^0/\text{Fe}_3\text{C}@\text{CS}$.

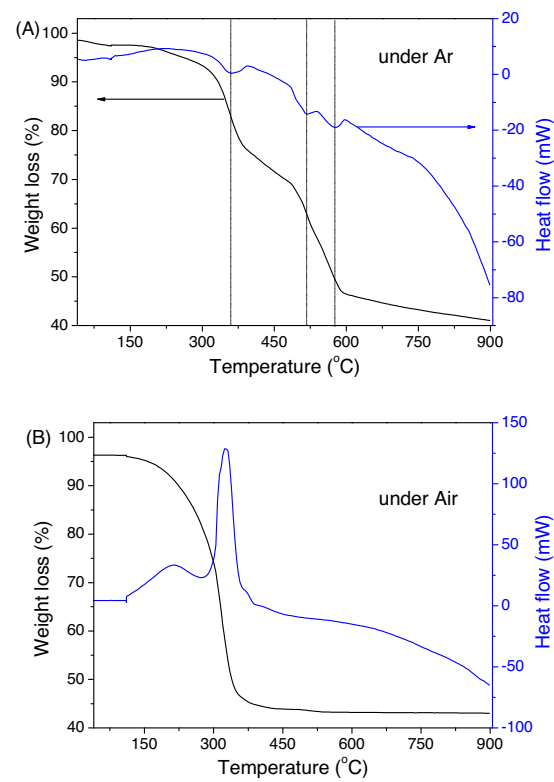


Fig. 4. TG-DSC profiles of $\text{Fe}^x@\text{CS}$ under (A) argon and (B) air.

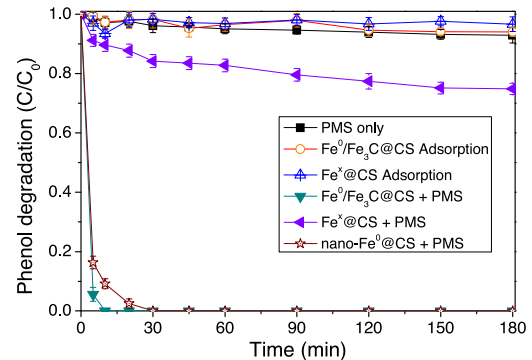


Fig. 5. Phenol removals in various conditions. Reaction conditions: $[\text{phenol}]_0 = 20 \text{ mg/L}$, catalyst loading = 0.2 g/L, oxone loading = 2.0 g/L, temperature: 25 °C.

At annealing temperature of 750 °C (Fig. S3(C)), the corresponding XPS Fe 2p spectrum was similar to that of $\text{Fe}^0/\text{Fe}_3\text{C}@\text{CS}$, and so were Fe^0 and Fe_3C levels. The increase of $\text{Fe}^0/\text{Fe}_3\text{C}$ ratio from 1.22 ($\text{Fe}^0/\text{Fe}_3\text{C}@\text{CS}$) to 1.50 ($\text{Fe}^x@\text{CS}-750$) might be ascribed to the reduction of Fe_2O_3 to Fe^0 at a higher annealing temperature. Due to the high Fe^0 composition, efficient phenol degradation was shown for the both catalysts.

To evaluate the effect of reaction conditions on catalytic phenol degradation, further studies were carried out by varying initial phenol concentration using $\text{Fe}^0/\text{Fe}_3\text{C}@\text{CS}$. Fig. 6 shows the effect of the initial phenol concentration on its catalytic degradation efficiency. A general trend can be observed that with increased initial phenol concentration, the time for 100% phenol degradation became longer. When the initial phenol concentration was increased from 20 to 40 and 60 ppm, 100% phenol degradation would require reaction duration at 10, 15 and 20 min, respectively.

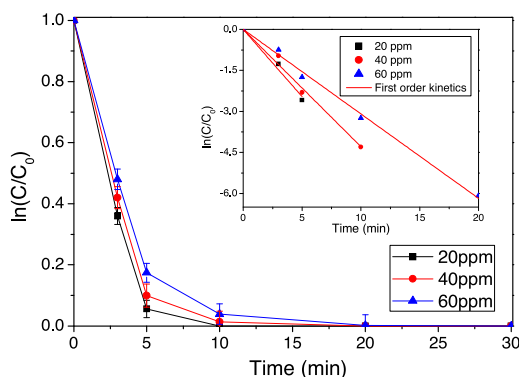


Fig. 6. Effect of phenol concentration on phenol degradation using $\text{Fe}^0/\text{Fe}_3\text{C}@\text{CS}$. Reaction conditions: catalyst loading = 0.1 g/L, oxone loading = 2.0 g/L, temperature: 25 °C.

For reaction kinetic studies, a first order kinetic model (Eq. (1)) was employed to evaluate the catalytic reaction kinetics.

$$\ln\left(\frac{c}{c_0}\right) = -kt \quad (1)$$

where c is the concentration of phenol at time (t) and c_0 is the initial phenol concentration. k is the first-order reaction rate constant. The inset of Fig. 6 shows that phenol degradation curves were well fitted by the first-order kinetics with high values of regressions coefficients. The reaction rate constants for the catalyst at three phenol concentrations are provided in Table 1. As seen, with the increase of the phenol concentration, the apparent rate constant (k) slightly decreased, indicating the decrease of the phenol degradation efficiency.

In the past few years, investigations have been carried out using ZVI for degradation of organic pollutants and most of the investigations have been using H_2O_2 [34–36], dissolved oxygen [37] and persulfate [34,38,39] to initiate the reactivity of ZVI. Lee et al. studied the effects of nano-ZVI/ H_2O_2 systems on conversion of methanol to HCHO using H_2O_2 as the oxidant [40]. They found that with the addition of 1 mM polyoxometalate (POM), 100 mM of methanol could be fully converted to HCHO within 180 min. Liang and Guo investigated oxidative and reductive pathways of ZVI catalysts in activating persulfate to degrade naphthalene [38]. They found that 10 ppm of naphthalene could be rapidly degraded by the ZVI activated persulfate within 120 min and sequential doses of small quantities of ZVI enhanced the naphthalene degradation efficiency. Recently, Sun et al. investigated ZVI activated peroxy-monosulfate (PMS) for phenol degradation and a superior catalytic activity of nanoscaled ZVI was observed compared with commercial ZVI and other metal catalysts [22]. This study presented similar reaction kinetics as the above.

Fig. 7 displays phenol degradation profiles on $\text{Fe}^0/\text{Fe}_3\text{C}@\text{CS}$ at varying temperatures. At elevated temperature, the phenol degradation rate was enhanced. The time for complete phenol degradation at 15, 25, and 35 °C was 60, 30 and 10 min, respectively. This trend implied the endothermic nature of the PMS activation process: higher temperature would stimulate PMS to generate reactive species more quickly for phenol degradation. Based on the first-order kinetics, reaction rate constants at varying temperatures were determined and the correlation between the rate constants

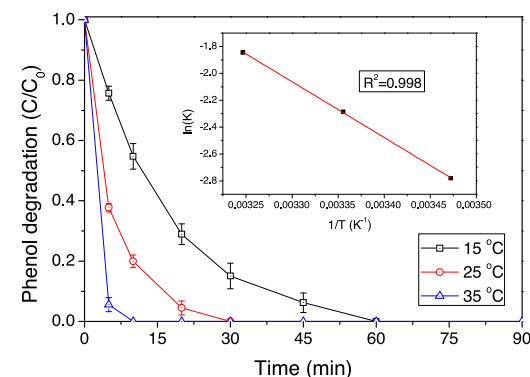


Fig. 7. Effect of reaction temperature on phenol degradation and estimation of activation energy. Reaction conditions: $[\text{phenol}]_0 = 20 \text{ mg/L}$, catalyst loading = 0.1 g/L, oxone® loading = 2.0 g/L.

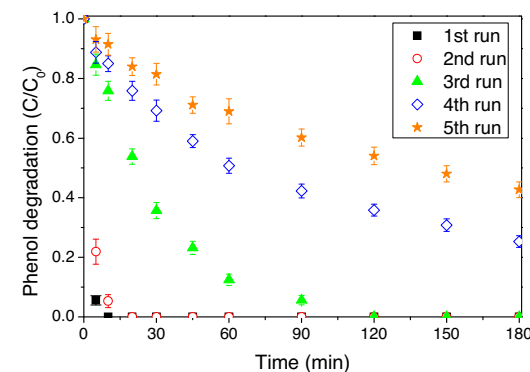


Fig. 8. Phenol degradation on $\text{Fe}^0/\text{Fe}_3\text{C}@\text{CS}$ at different runs for repeated uses. Reaction conditions: $[\text{phenol}]_0 = 20 \text{ mg/L}$, catalyst loading = 0.2 g/L, oxone® loading = 2.0 g/L, and $T = 25^\circ\text{C}$.

and reaction temperature was fitted well by the Arrhenius equation with a high regression coefficient, which is shown in the inset figure. The activation energy was then obtained to be 16.3 kJ/mol.

Fig. S4 shows photographs of $\text{Fe}^0/\text{Fe}_3\text{C}@\text{CS}$ dispersion in water and its response under an external magnetic field. It was found that $\text{Fe}^0/\text{Fe}_3\text{C}@\text{CS}$ could be well dispersed in water to form a stable black suspension after sonication for 1 min (Fig. S4(A)) and that the black suspension remained stable after 10 min (Fig. S4(B)). When a magnet approached, the catalyst accumulated quickly to the side wall near the magnet. And the solution became clear within 1 min (Fig. S4(C)). After the magnet was removed and as-mentioned sonication procedure was repeated, the $\text{Fe}^0/\text{Fe}_3\text{C}@\text{CS}$ sample was re-dispersed in water and formed the stable suspension again. Therefore, attraction and dispersion processes could be altered by an external magnetic field, and the as-synthesized $\text{Fe}^0/\text{Fe}_3\text{C}@\text{CS}$ demonstrated excellent water dispersion and magnetic separation for effective solid-solution separation.

3.3. Mechanism of enhanced reusability

The stability and recyclability of $\text{Fe}^0/\text{Fe}_3\text{C}@\text{CS}$ were investigated by successive reusability tests (Fig. 8). The catalysts were regenerated by simple water washing without any further treatment. In the reusability tests, the phenol degradation profile in the second run almost overlapped the first run indicating an excellent reusability. However, in the subsequent runs, the as-synthesized $\text{Fe}^0/\text{Fe}_3\text{C}@\text{CS}$ catalyst seemed to deactivate. For the third run, complete phenol removal occurred at 120 min which was much longer than the first and second runs. And for the 4th and 5th runs, around 30% and 50% phenol residue remained in solutions in 180 min. Although

Table 1
Kinetic parameters of $\text{Fe}^0/\text{Fe}_3\text{C}@\text{CS}$ in phenol degradation.

Catalyst	Phenol concentration (ppm)	k (min^{-1})	R^2 of k
$\text{Fe}^0/\text{Fe}_3\text{C}@\text{CS}$	20	0.58	0.989
	40	0.44	0.992
	60	0.31	0.997

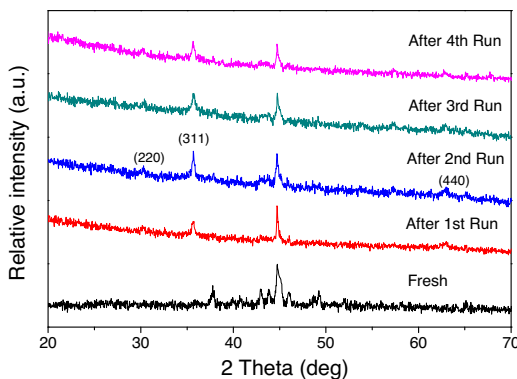


Fig. 9. XRD patterns of $\text{Fe}^0/\text{Fe}_3\text{C}@\text{CS}$ after each run.

deactivation occurred, the as-prepared catalyst still displayed notable catalytic activity even in the 5th run. The stability was much higher than nano- Fe^0 encapsulated in microcarbon spheres in the recent study [22], where the nano- $\text{Fe}^0@\text{CS}$ catalyst showed an inferior stability and deactivated dramatically from the second run. Compared with the nano- $\text{Fe}^0@\text{CS}$ in our previous study [22], the $\text{Fe}^0/\text{Fe}_3\text{C}@\text{CS}$ in this study presented significantly improved catalytic stability and reusability.

In order to probe the causes of deactivation, the catalyst from each test was collected and XRD analysis was then carried out. XRD patterns of $\text{Fe}^0/\text{Fe}_3\text{C}@\text{CS}$ after each run are shown in Fig. 9. As seen, compared with the fresh sample, diffraction peaks of $\gamma\text{-Fe}_2\text{O}_3$ (JCPDS card 39-1346) appeared, suggesting that some of the Fe^0 has been oxidized to $\text{Fe}(\text{III})$. Moreover, the peak intensity of Fe_3C also decreased on recycled catalyst from the 1st run, suggesting that besides Fe^0 was oxidized, some Fe_3C was also consumed during the catalytic reaction. However, unlike the Fe^0 after reaction with PMS [22], Fe_3C appeared to exist even after the fourth run. The stable Fe_3C phase might enable to maintain catalytic activity in the 5th run, as indicated in Fig. 8.

In order to further evaluate the changes on catalyst surface after uses and the deactivation mechanism, XPS study was carried out. XPS data of the fresh and the catalyst after 4th use are provided in Fig. 10. For XPS spectra of the fresh catalyst in the Fe 2p region (Fig. 10(A)), four characteristic peaks were identified. Binding energies of $\text{Fe} 2p_{1/2}$ (ca. 724 eV) and $\text{Fe} 2p_{3/2}$ (ca. 711 eV) were identified, referring to oxidized iron [$\text{Fe}(\text{III})$] [30,31]. The peaks at ca. 720 and 707 eV indicated the presence of the iron carbide (Fe_3C) and elemental iron (Fe^0) on the catalyst surface, respectively [32,33], which is in accordance with XRD analysis in Fig. 9.

The XPS O 1s (Fig. 10(B)) can be fitted into three components. The peak at ca. 529.9 eV was in agreement with the binding energy of O^{2-} , while the other peaks at ca. 531.2 and 534.5 eV could be indexed to OH^- and chemically/physically adsorbed water, respectively. The oxygen species were similar to those on the surface of iron oxides in water [33]. The presence of the oxidized iron suggests that nano ZVI (Fe^0) is extremely prone to being oxidized to $\text{Fe}(\text{III})$ even on the fresh catalyst.

For the catalyst obtained after the 4th use, XPS spectra were quite different. For XPS in Fe 2p region (Fig. 10(C)), the photoelectron peak of metal iron (ca. 707 eV) disappeared. Only two main photoelectron peaks were identified at ca. 724 and 711 eV, which can be ascribed to the oxidized $\text{Fe}(\text{III})$. While the peaks at 719 eV represents the binding energies of shake-up satellite $\text{Fe} 2p_{3/2}$ [30]. The disappearance of metal iron suggests that most of the Fe^0 on surface of the catalyst has been oxidized to $\text{Fe}(\text{III})$ during the catalytic reaction with PMS. The C1s spectrum of the used catalyst was also fitted with three components (Fig. 10(D)). The peak centered at ca. 283.6 eV confirmed the presence of Fe_3C [41], while the

other two peaks centered at 282.8 and 285.4 eV corresponded to the SiC and sp^3 -bonded carbon. The appearance of SiC might be resulted from the contamination brought by the calcination process. The integrated areas of these three peaks correspond to Fe_3C , SiC , and $\text{sp}^3\text{-C}$ contents were 65.6%, 24.4% and 11.5%, respectively, suggested that most of the carbon was in the form of iron carbide.

Based on XPS studies as well as XRD analysis, it can be concluded that, after catalytic reaction with PMS, most of surface elemental iron (Fe^0) was consumed and converted into $\gamma\text{-Fe}_2\text{O}_3$. However, iron carbide (Fe_3C) still remained, suggesting that the Fe_3C has a better stability than Fe^0 in catalytic reaction. Moreover, as shown in Fig. S5, the recycled catalyst after the 4th use still displayed similar magnetic behavior to the fresh sample, and the solution became clear within 1 min when approaching an external magnet. For the stability, in the first two runs, both Fe^0 and Fe_3C took part in catalytic reaction and the high reaction rate could be ascribed to the high catalytic activity of Fe^0 . With the repeating tests increase and depletion of the surface Fe^0 , reaction rates of phenol degradation decreased. At the 4th and 5th runs, the main component contributing to the catalytic reaction was iron carbide, because of the corrosion of Fe^0 (from XPS spectra) and the low catalytic activity of Fe_2O_3 in PMS activation [22]. In the catalytic processes, corrosion of Fe^0 will simultaneously occur with Fe^0 activation of PMS, while Fe_3C might act like metal oxide as a stable catalyst for a better stability. This is the first observation of Fe_3C catalysis in catalytic oxidation of organic pollutants. Though the insightful mechanism has not been very clear yet, it can be still concluded that, with introduction of melamine to the synthesis, Fe_3C was formed together with Fe^0 to improve both the activity and stability in phenol oxidation.

3.4. Mechanism of PMS activation and phenol degradation

Previous investigations have shown that homogeneous or heterogeneous activation of PMS could produce both hydroxyl radicals ($\cdot\text{OH}$) and sulfate radicals ($\text{SO}_4^{\cdot-}$) [6,42]. In order to investigate the generation processes of reactive species on $\text{Fe}^0/\text{Fe}_3\text{C}@\text{CS}$ activating PMS and the dominant species for phenol degradation, both EPR tests with DMPO as the spin trapping agent and the classical quenching tests were performed.

Our previous study showed that no peaks were identified when 6.5 mM PMS solution was tested without addition of DMPO or phenol solution, revealing that no electron spins could be captured without addition of spin-trapping agent [7]. With the addition of 20 ppm of phenol and 0.08 M of DMPO to PMS solution, characteristic signals of 5,5-dimethylpyrroline-(2)-oxyl-(1) (DMPOX) were identified, indicating that due to strong hydrolysis process of PMS, DMPO was directly oxidized to DMPOX [7,43]. When $\text{Fe}^0/\text{Fe}_3\text{C}@\text{CS}$ was added together with PMS (6.5 mM), DMPO (0.08 M) and phenol (20 ppm), both hydroxyl and sulfate radicals appeared by identification of the characteristic signals of DMPO- HO^{\cdot} and DMPO- $\text{SO}_4^{\cdot-}$ adducts, respectively.

Fig. 11 shows EPR spectra of reaction solution are dependent on reaction time. Within the first minute of the catalytic reaction, characteristic peaks of DMPO- HO^{\cdot} adducts (with hyperfine splitting constants of $a_N = a_H = 14.9$ G) and DMPO- $\text{SO}_4^{\cdot-}$ adducts (with hyperfine splitting constants of $a_N = 13.2$ G, $a_H = 9.6$ G, $a_H = 1.48$ G and $a_H = 0.78$ G) were observed, revealing both hydroxyl and sulfate radicals were generated at the very initial stage of the catalytic reaction [44]. However, the peak intensity of DMPO- $\text{SO}_4^{\cdot-}$ adducts was much weaker compared with that of DMPO- HO^{\cdot} adducts, indicating that concentration of sulfate radicals was much lower than that of hydroxyl radicals. When reaction time was prolonged to 4 min, the intensity of the DMPO- $\text{SO}_4^{\cdot-}$ adducts signal peak decreased. The decrease of the peak intensity indicated that the radicals generated by PMS activation have been quickly consumed by reacting

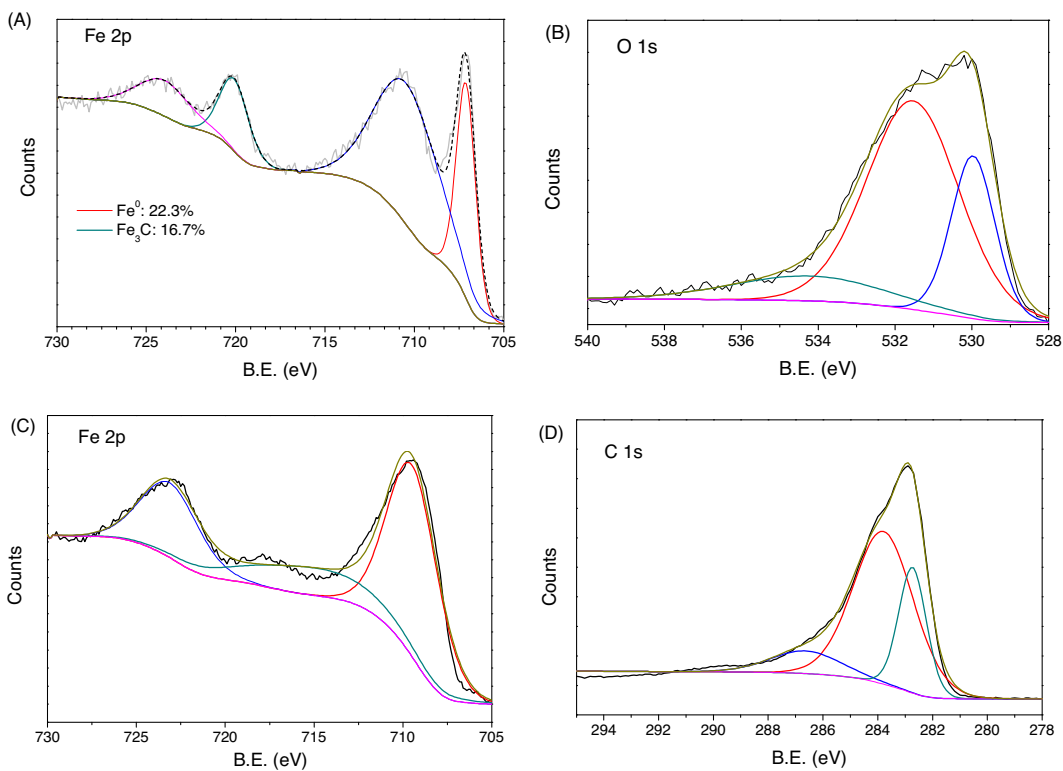


Fig. 10. XPS spectra of fresh/used catalysts. (A) XPS spectrum of Fe 2p region for fresh catalyst; (B) XPS spectrum of O 1s region for fresh catalyst; (C) XPS spectrum of Fe 2p region for 4th used catalyst; (D) XPS spectrum of C 1s region for 4th used catalyst.

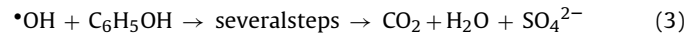
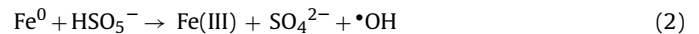
with phenol. However, when reaction time was extended to 9 min or longer (Fig. 11(B)), the peak intensity for DMPO- \cdot OH increased to higher values, suggesting that excessive hydroxyl radicals have been generated. While the peak intensity of DMPO- $\text{SO}_4^{\cdot-}$ remained roughly the same as the initial.

Fig. 12 shows relationship between phenol removal profile and evolution of the DMPO- \cdot OH/DMPO- $\text{SO}_4^{\cdot-}$ adduct peak intensities with time for $\text{Fe}^0/\text{Fe}_3\text{C}@\text{CS}$ catalyst. As seen, the relative intensity of hydroxyl radicals was much higher than that of sulfate radicals, while the unremarkable fluctuation in peak intensity of sulfate radicals happened during the catalytic reaction. These facts revealed that hydroxyl radicals were selectively produced during the PMS activation process. For variation of hydroxyl radicals, it reached the lowest point at 5 min, suggesting the fast consumption of the radicals since they have been generated. After that, their concentration increased significantly. Combined the DMPO- \cdot OH intensity variation with the phenol degradation profile, 80% of phenol degradation at the first 5 min could be accounted for the decreased hydroxyl radicals.

Our previous study showed that, when 3D MnO_2 was employed as the catalyst, both sulfate and hydroxyl radicals were generated during the PMS activation and the sulfate radicals dominated phenol oxidation process [7]. However, this study suggested that Fe metal-based catalysts could generate different radicals during PMS activation process for phenol oxidation. To further investigate the dominant radical species responsible for phenol degradation, classical quenching tests employing ethanol (EtOH) and tert-butyl alcohol (TBA) as quenching agents were carried out. It is well accepted that $\text{SO}_4^{\cdot-}$ is selective to be quenched more rapidly by a quenching agent with α -hydrogen and the reaction rates of $\text{SO}_4^{\cdot-}$ with EtOH (with α -hydrogen) and TBA (without α -hydrogen) are $1.6 \times 10^7 - 7.7 \times 10^7$ and $4.0 \times 10^5 - 9.1 \times 10^5 \text{ M}^{-1} \text{ s}^{-1}$, respectively [45,46]. While both

EtOH and TBA could sufficiently quench $\cdot\text{OH}$ with the rates of $1.2 \times 10^9 - 2.8 \times 10^9$ and $3.8 \times 10^8 - 7.6 \times 10^8 \text{ M}^{-1} \text{ s}^{-1}$, respectively [45].

Fig. 13 shows the change of reaction rate constant (k) in quenching tests. When 0.2 M EtOH was added, the reaction rate reduced from 0.27 to 0.17 min^{-1} , indicating that some portions of hydroxyl and sulfate radicals were quenched during the catalytic reaction. When 0.2 M TBA was added to the original reaction solution, reaction rate decreased to around 0.15 min^{-1} , which was roughly the same as that by addition of EtOH. By combination of the EPR spectra variation and the results of the classical quenching tests, it was concluded that hydroxyl radicals were selectively generated against sulfate radicals during the heterogeneous PMS activation process. Because solid PMS is facile for transportation and storage, then it could be used as an alternate to hydrogen peroxide employed in homogenous Fenton reaction. Moreover, it was also deduced that hydroxyl radicals are dominating phenol degradation. And the mechanisms of PMS activation on $\text{Fe}^0/\text{Fe}_3\text{C}@\text{CS}$ for phenol degradation can be proposed as follows.



In this study, $\text{Fe}^0/\text{Fe}_3\text{C}$ based nano hybrids demonstrated efficient catalytic activation of PMS for degradation of organic pollutants, in which Fe_3C catalysis was discovered for the very first time. Besides its use for decomposition of aqueous organic pollutants, $\text{Fe}^0/\text{Fe}_3\text{C}$ based nanomaterials have been employed in reduction and adsorption of heavy metals. López et al. [47] prepared $\text{Fe}/\text{Fe}_3\text{C}$ ultrafine particles and compared their adsorption of Se(IV) with Fe_3O_4 nanoparticles. They found that $\text{Fe}/\text{Fe}_3\text{C}$ NPs were superior to Fe_3O_4 NPs because of the ability in immobilization of Se(IV) rapidly and irreversibly via a reductive mechanism. Wang

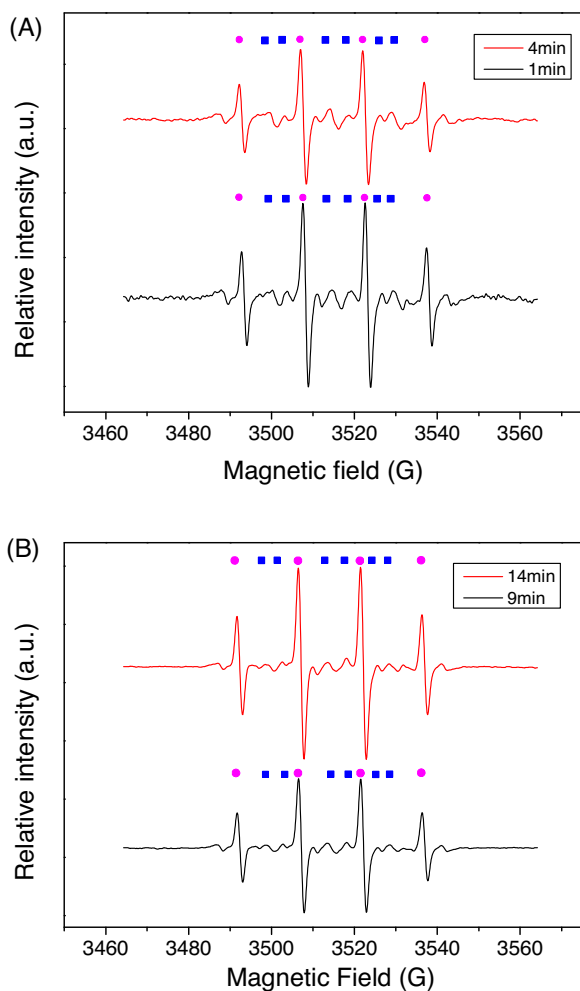


Fig. 11. EPR spectra in various conditions. Centerfield: 3512 G; sweep width: 100 G; microwave frequency: 9.87 GHz; modulation frequency: 100 GHz; and power: 18.11 mW. Reaction condition: phenol = 20 ppm; catalyst loading = 0.1 g/L; PMS loading = 6.5 mM, pH 7.0; DMPO = 0.08 M. DMPO-•OH; DMPO-SO₄²⁻.

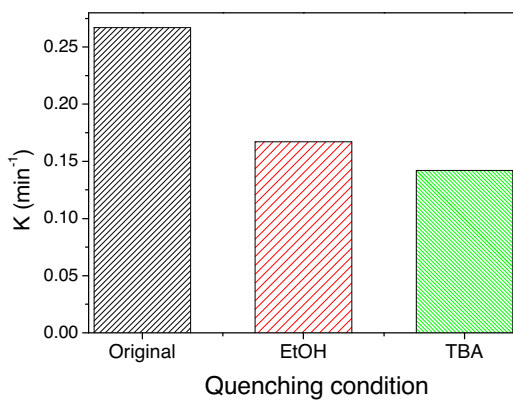


Fig. 13. Changes of reaction rate (k) of catalysts with and without quenching agents of EtOH (0.2 M) and TBA (0.2 M). Reaction conditions: phenol = 20 mg/L, catalyst loading = 0.1 g/L, oxone loading = 6.5 mM, and T = 25 °C.

et al. [48] prepared Fe/Fe₃C@porous carbon sheets via biomass and used for simultaneous reduction and adsorption of uranium (VI) for aqueous solution. It can be expected that such Fe⁰/Fe₃C hybrids in this study can also be employed to remove both organic pollutants and toxic heavy metals in water, which will be investigated in near future.

4. Conclusions

Fe⁰/Fe₃C@CS nanocomposites were synthesized via a modified hydrothermal method followed by self-reduction under heated nitrogen atmosphere. The addition of melamine appeared to enable the formation of an additional phase of Fe₃C along with Fe⁰. The novel ZVI-based nanocomposites showed a superior catalytic activity in activation of PMS for phenol degradation. The kinetic studies suggested that, in the heterogeneous systems, catalytic oxidation of phenol followed first order kinetics and the apparent activation energy was 16.3 kJ/mol. Moreover, Fe₃C catalysis for PMS activation was observed for the first time though detailed catalytic mechanism is still not very clear at the current stage. The catalyst deactivation mechanism was also investigated and it was found that Fe₃C has a better catalytic stability than Fe⁰ in catalytic reaction. Magnetic separation was also remained even after five runs. The combination of EPR analysis and quenching tests showed that hydroxyl radicals were generated selectively against sulfate radicals within the PMS activation process and thus responsible for phenol oxidation. This study provided a feasible approach for removal of organic pollutants by magnetically separable catalysts via advanced material design.

Acknowledgements

The authors acknowledge the use of equipment, scientific and technical assistance of the Curtin University Electron Microscope Facility and Centre for Microscopy Characterization, which has been partially funded by the University, State and Commonwealth Governments. H.S. is grateful for the supports of Curtin Research Fellowship and Opening Project (KL13-02) of State Key Laboratory of Materials-Oriented Chemical Engineering, China.

Appendix A. Supplementary data

Supplementary data associated with this article can be found, in the online version, at <http://dx.doi.org/10.1016/j.apcatb.2015.02.016>.

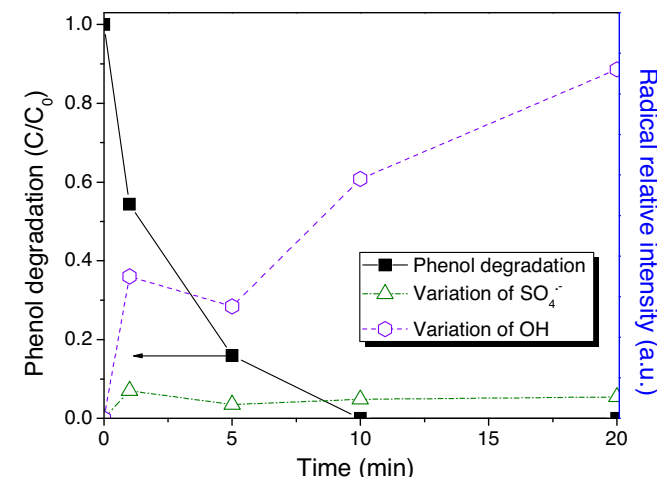


Fig. 12. Phenol removal profile and intensity variations of DMPO-•OH and DMPO-SO₄²⁻ during reaction on Fe⁰/Fe₃C@CS. Reaction conditions: phenol = 20 mg/L; catalyst loading = 0.1 g/L; PMS loading = 6.5 mM, pH 7.0.

References

[1] P. Bautista, A.F. Mohedano, J.A. Casas, J.A. Zazo, J.J. Rodriguez, *J. Chem. Technol. Biotechnol.* 83 (2008) 1323–1338.

[2] E. Neyens, J. Baeyens, *J. Hazard. Mater.* 98 (2003) 33–50.

[3] S. Wang, *Dyes Pigm.* 76 (2008) 714–720.

[4] L. Hu, X. Yang, S. Dang, *Appl. Catal. B* 102 (2011) 19–26.

[5] G.P. Anipsitakis, D.D. Dionysiou, *Environ. Sci. Technol.* 38 (2004) 3705–3712.

[6] G.P. Anipsitakis, D.D. Dionysiou, *Environ. Sci. Technol.* 37 (2003) 4790–4797.

[7] Y. Wang, H. Sun, H.M. Ang, M.O. Tadé, S. Wang, *Appl. Catal. B* 164 (2015) 159–167.

[8] H.Q. Sun, Y.X. Wang, S.Z. Liu, L. Ge, L. Wang, Z.H. Zhu, S.B. Wang, *Chem. Commun.* 49 (2013) 9914–9916.

[9] E. Saputra, S. Muhammad, H.Q. Sun, H.M. Ang, M.O. Tade, S.B. Wang, *Environ. Sci. Technol.* 47 (2013) 5882–5887.

[10] H.Q. Sun, S.Z. Liu, G.L. Zhou, H.M. Ang, M.O. Tade, S.B. Wang, *ACS Appl. Mater. Interfaces* 4 (2012) 5466–5471.

[11] D. O'Carroll, B. Sleep, M. Krol, H. Boparai, C. Kocur, *Adv. Water Res.* 51 (2013) 104–122.

[12] R.A. Crane, T.B. Scott, *J. Hazard. Mater.* 211–212 (2012) 112–125.

[13] A. Ryu, S.-W. Jeong, A. Jang, H. Choi, *Appl. Catal. B* 105 (2011) 128–135.

[14] H. Song, E.R. Carraway, *Environ. Sci. Technol.* 39 (2005) 6237–6245.

[15] A. Rastogi, S.R. Al-Abed, D.D. Dionysiou, *Appl. Catal. B* 85 (2009) 171–179.

[16] H. Liu, J. Xu, Y. Li, *Acc. Chem. Res.* 43 (2010) 1496–1508.

[17] Y. Li, Y. Zhang, J. Li, X. Zheng, *Environ. Pollut.* 159 (2011) 3744–3749.

[18] Z.-X. Chen, X.-Y. Jin, Z. Chen, M. Megharaj, R. Naidu, *J. Colloid Interface Sci.* 363 (2011) 601–607.

[19] H. Zhu, Y. Jia, X. Wu, H. Wang, *J. Hazard. Mater.* 172 (2009) 1591–1596.

[20] D. Karabelli, S. Ünal, T. Shahwan, A.E. Eroğlu, *Chem. Eng. J.* 168 (2011) 979–984.

[21] Z. Jiang, L. Lv, W. Zhang, Q. Du, B. Pan, L. Yang, Q. Zhang, *Water Res.* 45 (2011) 2191–2198.

[22] H.Q. Sun, G.L. Zhou, S.Z. Liu, H.M. Ang, M.O. Tade, S.B. Wang, *ACS Appl. Mater. Interfaces* 4 (2012) 6235–6241.

[23] M. Fardis, A.P. Douvalis, D. Tsitrouli, I. Rabias, D. Stamopoulos, K. Th, E. Karakosta, G. Diamantopoulos, T. Bakas, G. Papavassiliou, *J. Phys. Condens. Matter* 24 (2012) 156001.

[24] G. Dong, K. Zhao, L. Zhang, *Chem. Commun.* 48 (2012) 6178–6180.

[25] L. Wang, C. Tian, B. Wang, R. Wang, W. Zhou, H. Fu, *Chem. Commun.* (2008) 5411–5413.

[26] Y. Li, R. Yi, A. Yan, L. Deng, K. Zhou, X. Liu, *Solid State Sci.* 11 (2009) 1319–1324.

[27] P. Zhang, Y. Zhan, B. Cai, C. Hao, J. Wang, C. Liu, Z. Meng, Z. Yin, Q. Chen, *Nano Res.* 3 (2010) 235–243.

[28] M. Feyzi, M. Irandoost, A.A. Mirzaei, *Fuel Process. Technol.* 92 (2011) 1136–1143.

[29] H. Sun, H. Tian, Y. Hardjono, C.E. Buckley, S. Wang, *Catal. Today* 186 (2012) 63–68.

[30] Y.-P. Sun, X.-Q. Li, J. Cao, W.-X. Zhang, H.P. Wang, *Adv. Colloid Interface Sci.* 120 (2006) 47–56.

[31] P. Mondal, S. Bhowmick, N. Jullock, W. Ye, W. Van Renterghem, S. Van den Berghe, B. Van der Bruggen, *J. Phys. Chem. C* 118 (2014) 21614–21621.

[32] Y. Liang, P. Liu, J. Xiao, H. Li, C. Wang, G. Yang, *Sci. Rep.* 3 (2013), Article number: 3051.

[33] X.-Q. Li, D.W. Elliott, W.-X. Zhang, *Crit. Rev. Solid State Mater. Sci.* 31 (2006) 111–122.

[34] T. Zhou, Y. Li, J. Ji, F.-S. Wong, X. Lu, *Sep. Purif. Technol.* 62 (2008) 551–558.

[35] M. Kallel, C. Belaid, R. Boussahel, M. Ksibi, A. Montiel, B. Elleuch, *J. Hazard. Mater.* 163 (2009) 550–554.

[36] R. Boussahel, D. Harik, M. Mammar, S. Lamara-Mohamed, *Desalination* 206 (2007) 369–372.

[37] D.-H. Kim, J. Kim, W. Choi, *J. Hazard. Mater.* 192 (2011) 928–931.

[38] C. Liang, Y.-Y. Guo, *Environ. Sci. Technol.* 44 (2010) 8203–8208.

[39] H. Kusic, I. Peternel, S. Ukić, N. Koprivanac, T. Bolanca, S. Papic, A.L. Božić, *Chem. Eng. J.* 172 (2011) 109–121.

[40] J. Jiang, S.-Y. Pang, J. Ma, *Environ. Sci. Technol.* 42 (2008) 8167–8168.

[41] H. Goretzki, P.V. Rosenstiel, S. Mandziej, Z. Fresenius, *Anal. Chem.* 333 (1989) 451–452.

[42] E. Saputra, S. Muhammad, H. Sun, H.-M. Ang, M.O. Tadé, S. Wang, *Appl. Catal. B* 142–143 (2013) 729–735.

[43] R.A. Floyd, L.M. Soong, *Biochem. Biophys. Res. Commun.* 74 (1977) 79–84.

[44] G.-D. Fang, D.D. Dionysiou, S.R. Al-Abed, D.-M. Zhou, *Appl. Catal. B* 129 (2013) 325–332.

[45] G.V. Buxton, C.L. Greenstock, W.P. Helman, A.B. Ross, *J. Phys. Chem. Ref. Data* 17 (1988) 513–886.

[46] P. Neta, R.E. Huie, A.B. Ross, *J. Phys. Chem. Ref. Data* 17 (1988) 1027–1284.

[47] R. López de Arroyabe Loyo, S.I. Nikitenko, A.C. Scheinost, M. Simonoff, *Environ. Sci. Technol.* 42 (2008) 2451–2456.

[48] X. Wang, S. Zhang, J. Li, J. Xu, X. Wang, *Inorg. Chem. Front.* 1 (2014) 641–648.